# High-salt diet suppresses autoimmune demyelination by regulating the blood–brain barrier permeability

Shin-Young Na[a], Mathangi Janakiraman[a], Alexei Leliavski[a], and Gurumoorthy Krishnamoorthy[a,1]

[a]Research Group Neuroinflammation and Mucosal Immunology, Max Planck Institute of Biochemistry, 82152 Martinsried, Germany

Edited by Lawrence Steinman, Stanford University School of Medicine, Stanford, CA, and approved February 16, 2021 (received for review December 16, 2020)

**Sodium chloride, "salt," is an essential component of daily food and vitally contributes to the body's homeostasis. However, excessive salt intake has often been held responsible for numerous health risks associated with the cardiovascular system and kidney. Recent reports linked a high-salt diet (HSD) to the exacerbation of artificially induced central nervous system (CNS) autoimmune pathology through changes in microbiota and enhanced $T_H17$ cell differentiation [M. Kleinewietfeld *et al.*, *Nature* 496, 518–522 (2013); C. Wu *et al.*, *Nature* 496, 513–517 (2013); N. Wilck *et al.*, *Nature* 551, 585–589 (2017)]. However, there is no evidence that dietary salt promotes or worsens a spontaneous autoimmune disease. Here we show that HSD suppresses autoimmune disease development in a mouse model of spontaneous CNS autoimmunity. We found that HSD consumption increased the circulating serum levels of the glucocorticoid hormone corticosterone. Corticosterone enhanced the expression of tight junction molecules on the brain endothelial cells and promoted the tightening of the blood–brain barrier (BBB) thereby controlling the entry of inflammatory T cells into the CNS. Our results demonstrate the multifaceted and potentially beneficial effects of moderately increased salt consumption in CNS autoimmunity.**

multiple sclerosis | dietary salt | experimental autoimmune encephalomyelitis

Excess salt (sodium chloride; NaCl) intake is associated with elevated blood pressure. However, the optimal range of sodium intake for cardiovascular health is controversial. A drastic reduction of salt intake is widely considered as a logical therapeutic consequence (4), a stand, which has not been met with unreserved acclaim (5).

Dietary salt intake has also been considered as an important risk factor for autoimmune diseases like multiple sclerosis (MS), whose incidence is steadily increasing in the last few decades. However, evidence that sodium intake is directly associated with MS pathogenesis is controversial (6, 7). Previous reports found that in actively induced experimental autoimmune encephalomyelitis (active EAE), a mouse model of MS, a high-salt diet (HSD) drives T cell differentiation toward proinflammatory pathogenic $T_H17$ cells and exacerbates clinical disease (1–3). It is important to note that the active EAE model used in these studies substantially differs from MS in regards to the disease initiation phase. Indeed, active EAE is induced by immunization with autoantigen and immune-activating microbial adjuvants (complete Freund's adjuvant [CFA] plus pertussis toxin). This protocol allows simultaneous activation and expansion of naïve T cells and the opening of the blood–brain barrier (BBB) by pertussis toxin to facilitate the entry of activated T cells into the central nervous system (CNS). However, similar processes of T cell activation or the opening of the BBB through immunization are unknown in MS patients. In fact, vaccination against tetanus, hepatitis B, or influenza does not correlate with the onset of MS, or with relapses of the disease (8).

Here, we evaluated the effects of an HSD on early pathogenic events that are necessary for the initiation of CNS autoimmunity using a spontaneous EAE mouse model. Against expectation, an HSD profoundly protected spontaneous EAE development. High salt altered the hormonal balance by interfering with the metabolism of corticosterone. The increased corticosterone levels induced the higher expression of BBB tight junction molecules to limit the infiltration of immune cells into the CNS. Collectively, our data suggest that moderate elevation of salt uptake might be beneficial in CNS autoimmunity.

## Results and Discussion

We examined the effect of HSD on spontaneously developing autoimmune demyelinating disease using the transgenic opticospinal encephalomyelitis (OSE) mouse that harbors myelin-reactive T and B cells in their immune repertoire (9). Within 4 mo, about 50% of OSE mice spontaneously develop a monophasic autoimmune disease (9). In our initial experiments, we compared the disease incidence of OSE mice that were raised (from birth) on a control rodent chow diet or an HSD containing 4% NaCl, along with autoclaved water ad libitum. Unexpectedly, we noted a significant reduction in the incidence of neurological symptoms in HSD-fed OSE mice. While ∼40% of chow-fed OSE mice developed spontaneous EAE within 4 mo, less than 9% of HSD-fed mice developed spontaneous EAE (Fig. 1*A*).

In the above experiment, we started HSD treatment in breeding pairs, since our experience with the OSE mouse model showed that about 5 to 10% of mice develop spontaneous EAE within 2 wk after weaning. To determine if the autoimmune disease suppression by HSD is due to any unexpected physiological changes in early developmental life, we also performed diet switch experiments after weaning. We raised OSE mice on a chow diet, weaned them onto HSD, and followed these mice for spontaneous EAE signs. Again, we observed significant disease protection in mice that were switched to HSD compared to mice kept on a chow diet (Fig. 1*B*). Since the chow diet is a crude cereal-based diet whose components differ from purified components in HSD,

### Significance

**Dietary salt intake has been considered an important risk factor for autoimmune diseases like multiple sclerosis (MS). Here we studied the effects of a high-salt diet (HSD) using a spontaneous autoimmune disease mouse model resembling MS. We found that high-salt consumption protects mice from developing the neurological disease by promoting the tightening of the blood–brain barrier and preventing the migration of autoreactive T cells into the CNS. Our results emphasize the multifarious effects of high-salt consumption in autoimmune disease susceptibility.**

Author contributions: S.-Y.N., M.J., and G.K. designed research; S.-Y.N., M.J., and G.K. performed research; S.-Y.N., M.J., A.L., and G.K. analyzed data; and S.-Y.N., M.J., A.L., and G.K. wrote the paper.

The authors declare no competing interest.

This article is a PNAS Direct Submission.



[1]To whom correspondence may be addressed. Email: guru@biochem.mpg.de.

This article contains supporting information online at https://www.pnas.org/lookup/suppl/doi:10.1073/pnas.2025944118/-/DCSupplemental.

Published March 15, 2021.

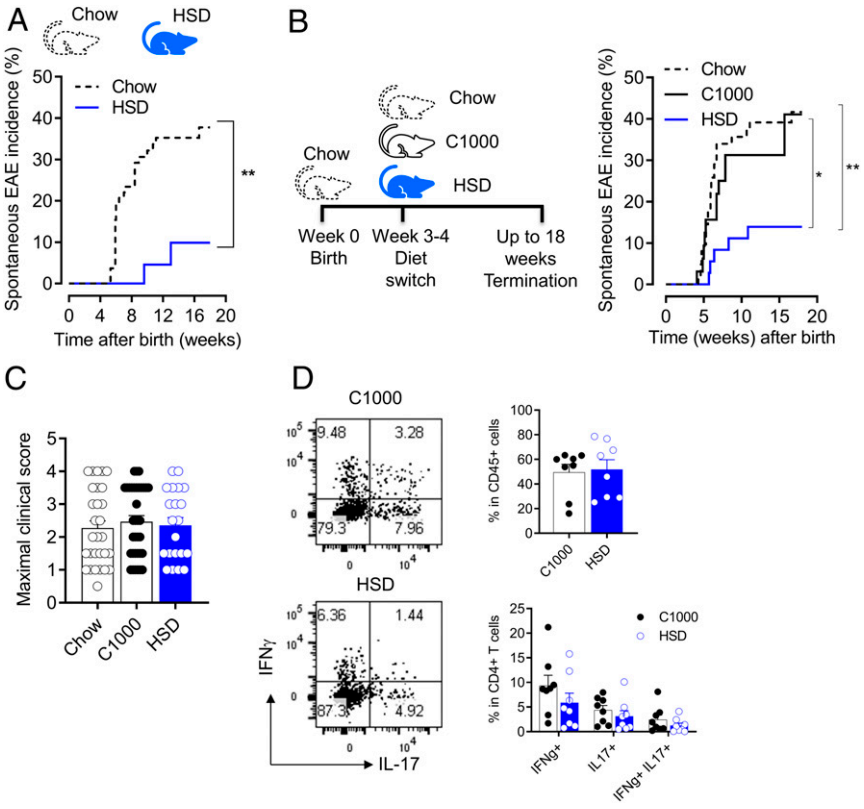


**Fig. 1.** High-salt intake suppresses spontaneous EAE. (*A*) Incidence of spontaneous EAE in OSE mice raised on chow ($n = 89$) or HSD ($n = 22$) from their birth. $^{**}P = 0.0083$ (Gehan–Breslow–Wilcoxon test). (*B*) Experimental scheme and incidence of spontaneous EAE in OSE mice fed chow ($n = 62$), C1000 ($n = 32$), or HSD ($n = 36$). Mice were switched to the respective diets at weaning. $^{*}P = 0.0412$; $^{**}P = 0.0028$ (Gehan–Breslow–Wilcoxon test). (*C*) Maximal clinical scores attained by chow ($n = 29$)-, C1000 ($n = 35$)-, and HSD ($n = 21$)-fed OSE mice that developed EAE symptoms. Mice were switched to the respective diets at weaning. Each circle represents an individual mouse. (*D*) Flow cytometry analysis of spinal cord-infiltrating T cell populations in C1000 ($n = 8$)- and HSD ($n = 8$)-fed OSE mice with spontaneous EAE. Frequencies of total $CD4^+$ T cells (*Top Right*) and $IFN\gamma^+$, $IL\text{-}17^+$, and $IFN\gamma^+IL\text{-}17^+$ T cells (*Bottom Right*) are depicted. Representative plots are shown on the *Left*. Each circle represents an individual mouse. (*A–C*) The combined data from more than five litters of mice are shown. (*D*) The combined data from two independent experiments are shown.

we performed additional experiments with a purified control diet (C1000). In this experimental paradigm as well, HSD significantly suppressed spontaneous EAE development, while no detectable differences were observed in spontaneous EAE incidence between C1000- and chow diet-fed OSE mice (Fig. 1*B*). However, HSD did not affect the severity of the disease in those mice that developed EAE symptoms, and CNS infiltrating cytokine-producing T cells were comparable (Fig. 1 *C* and *D*). These results suggest that HSD controls the early pathogenic processes that are essential for immune cell entry into the CNS but do not control the autoimmune reactivity within the CNS.

The CNS autoimmune disease protection by HSD was surprising and is in contrast to the previous reports, which showed that HSD aggravated EAE in the active EAE model induced in wild-type (WT) C57BL/6 mice (1–3). We, therefore, immunized WT C57BL/6 mice fed a C1000 or HSD with myelin oligodendrocyte glycoprotein peptide 35 to 55 ($MOG_{35–55}$) in CFA plus pertussis toxin. In our hands, we observed neither disease protection nor an exacerbation of EAE (*SI Appendix*, Fig. S1*A*). One difference between our study and the published studies is the supplementation of 1% salt in drinking water along with 4% salt in the food pellets. This dietary regimen also had no impact on the active EAE disease course (*SI Appendix*, Fig. S1*A*), despite a comparable increase of sodium in urine samples (*SI Appendix*, Fig. S1*B*). We also did not find quantitative differences in the pathogenic T cell infiltrates of the CNS (*SI Appendix*, Fig. S1*C*). Overall, our data indicate that HSD suppresses spontaneous EAE but has no impact on the artificially induced EAE.

To identify the mechanisms of HSD-mediated protection from spontaneous EAE, we first focused on potential alterations within the immune system, since EAE results from the invasion of activated pathogenic autoreactive T cells from the periphery into the CNS. As in previous studies (1–3), we noted that HSD significantly increased the frequencies of $T_H17$ cells in the small intestine but not in the colon of OSE mice (Fig. 2*A*). The frequencies of $T_H17$ cells were also slightly increased in the spleen but did not reach statistical significance (Fig. 2*A*). The frequencies of IFNγ-producing $T_H1$ cells or $Foxp3^+$ regulatory T ($T_{reg}$) cells remained similar (Fig. 2*A*). We did not notice any appreciable changes in the overall frequencies of other immune cell types in the intestine and spleen (*SI Appendix*, Fig. S2*A*). Although $T_{reg}$ cell frequencies were similar in HSD- and C1000-fed mice, we investigated if they were functionally different. $T_{reg}$ cells sorted from HSD-fed mice had a comparable suppressive capacity to that of controls (*SI Appendix*, Fig. S2*B*). Furthermore, depletion of $T_{reg}$ cells with anti-CD25 antibodies did not appreciably affect the disease incidence in HSD-fed OSE mice (*SI Appendix*, Fig. S2*C*). In OSE mice, spontaneous EAE development critically depends on the bidirectional cooperation between antigen-specific T and B cells (9). We, therefore, examined the antibody levels and the functional capacity of B cells to activate T cells. B cells from both HSD- and C1000-fed mice had a similar capacity to present antigen to the T cells and proliferated comparably (Fig. 2*B*). The total and MOG-specific antibody titers in the serum of OSE mice were also similar (*SI Appendix*, Fig. S3). Thus, we conclude that HSD induces the

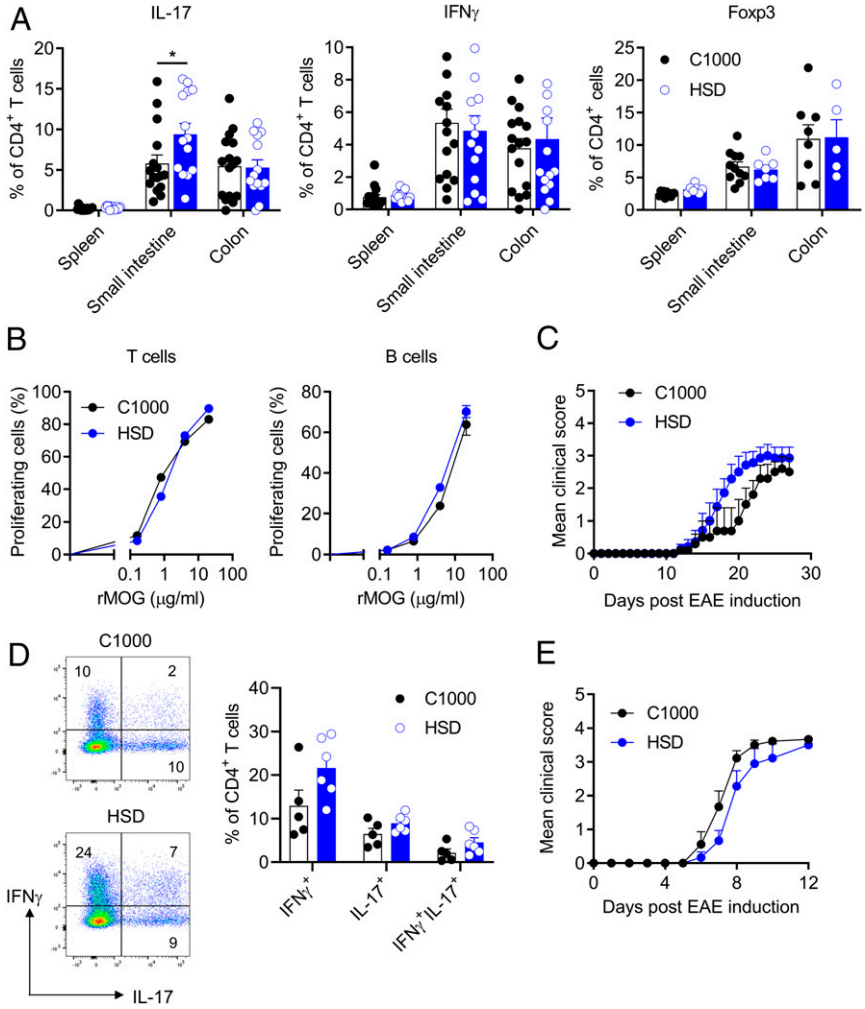


**Fig. 2.** High-salt diet does not affect the encephalitogenic capacity of T cells. (*A*) Flow cytometry analysis of IL-17$^+$, IFNγ$^+$, and Foxp3$^+$ T cell frequencies in the spleen, small intestine, and colonic lamina propria of C1000 ($n$ = 8 to 16)- and HSD ($n$ = 5 to 14)-fed OSE mice. The combined data from three independent experiments are shown. For IL-17 and IFNγ and for Foxp3 in the spleen and small intestine, each circle represents an individual mouse. For Foxp3 in the colon, each circle represents a pool of two mice. *$P$ = 0.0275 (Mann–Whitney $U$ test, two tailed). (*B*) Proliferation of T cells and B cells in the presence of antigen. Splenocytes from OSE mice fed C1000 ($n$ = 6) or HSD ($n$ = 7) were labeled and stimulated with increasing concentrations of recombinant MOG. Frequencies of proliferating CD4$^+$ T lymphocytes and B220$^+$ B lymphocytes are shown. Representative data from three independent experiments are shown. (*C*) Mean EAE clinical scores of *Rag2*$^{-/-}$ mice that received splenocytes from OSE mice fed C1000 ($n$ = 5) or HSD ($n$ = 7). The combined data from two independent experiments are shown. (*D*) Flow cytometry analysis of spinal cord-infiltrating T cell populations from *Rag2*$^{-/-}$ mice that developed EAE after receiving splenocytes from OSE mice fed C1000 ($n$ = 5) or HSD ($n$ = 6). Representative plots are shown on the *Left*. The frequencies of IFNγ$^+$, IL-17$^+$, and IFNγ$^+$IL-17$^+$ T cells are shown on the *Right*. The combined data from two independent experiments are shown. Each circle represents an individual mouse. (*E*) Mean EAE clinical scores in OSE mice fed C1000 ($n$ = 9) or HSD ($n$ = 9) and immunized with $MOG_{35–55}$ in CFA and pertussis toxin. The combined data from two independent experiments are shown.

expansion of IL-17 producing T cells, without a significant impact on the numbers and functional properties of B cells or regulatory T cells.

Expansion of $T_H17$ cells in mice protected from EAE may appear paradoxical, considering the well-established function of $T_H17$ cells as the main autoimmune effectors in actively induced EAE models (10). However, it should be noted that $T_H17$-like cells and their secreted cytokine, IL-17, have conflicting effects on the immune system. The functional heterogeneity of murine $T_H17$ cells critically depends on the priming conditions both in vitro and in vivo (11, 12). For example, in the ileal lamina propria, $T_H17$ cells may be reeducated to acquire an anti-inflammatory phenotype (13). Also, a recent report suggests that human $T_H17$ cells (CD4$^+$CD14$^-$CD45RA$^-$CCR6$^+$CCR4$^+$CXCR3$^-$) cultured in vitro under high-salt conditions assume an anti-inflammatory phenotype characterized by the up-regulation of Foxp3 and IL-10 (14). However, we neither found changes in the Foxp3 expression (Fig. 2*A*) nor in IL-10 production from T cells from OSE mice fed an HSD. To determine if the HSD-induced $T_H17$ cells are responsible for disease protection, we transferred spleen cells from HSD- and C1000-fed OSE mice into *Rag2*$^{-/-}$ recipients. Splenocytes from HSD-fed OSE mice were capable of triggering disease similar to those from OSE mice kept on the C1000 diet (Fig. 2*C*). Analysis of CNS infiltrates showed no differences in the frequencies of IL-17- and IFNγ-producing T cells (Fig. 2*D*). Moreover, immunization of disease-resistant HSD-fed OSE mice with $MOG_{35–55}$ plus pertussis toxin resulted in comparable clinical EAE scores (Fig. 2*E*). These results suggest that HSD-induced in vivo expanded $T_H17$ cells do not have an anti-inflammatory phenotype and are fully functional, capable of driving autoimmune disease upon activation by external stimuli.

We reasoned that the discrepancy in the disease manifestation in HSD-fed mice between active EAE and spontaneous EAE models might be the consequence of altered BBB properties. In

fact, pertussis toxin used in the active EAE models is known to alter the BBB permeability and facilitate T cell migration into the CNS. Western blot analysis showed an increased expression of BBB junctional molecules ZO-1 and claudin-5 in the brain endothelial cells isolated from HSD-fed OSE mice and WT C57BL/6 mice (Fig. 3*A* and *SI Appendix*, Fig. S4). To identify the mechanisms behind these changes, we focused our investigations on circulating components with the potential to alter BBB. High-salt intake is known to induce changes in mineralocorticoid and glucocorticoid levels in both mice and humans (15–18). We detected elevated levels of corticosterone in the serum of HSD-fed OSE mice (Fig. 3*B*). The glucocorticoid hormone, corticosterone, along with the mineralocorticoid hormone, aldosterone, is involved in the regulation of sodium homeostasis. Although corticosterone is primarily produced in the adrenal cortex, it may also be synthesized by nonadrenal tissues including intestinal epithelium (19, 20). The intestinal corticosterone production was found to be elevated in germ-free and antibiotics-treated mice, suggesting the contribution of microbiota in the induction of steroidogenic enzymes (21). However, we found changes neither in corticosterone nor in the adrenocortical biosynthetic pathway gene expression levels in the intestine, ruling out the role of microbiota in regulating the corticosterone production in HSD-fed OSE mice (*SI Appendix*, Fig. S5). In the adrenal glands, the expression of the steroidogenic enzymes *Cyp11a1*, *Hsd3b1*, *Cyp21a1*, *Cyp11b1*, and *Hsdb11* was similar in C1000- and HSD-fed OSE mice. However, the expression levels of *Cyp11b2* (aldosterone synthase), which converts corticosterone to aldosterone, were significantly reduced (Fig. 3*C* and *SI Appendix*, Fig. S6) suggesting that elevated serum corticosterone in HSD-fed mice might be the consequence of diminished metabolism of corticosterone.

Next, we examined the effects of corticosterone on BBB endothelial cells. Transcriptomics and quantitative proteomics analyses showed that, along with known glucocorticoid-responsive genes (*Fkbp5*, *Sgk1*, and *Dusp1*), corticosterone treatment of brain endothelioma cell line bEnd.3 cells significantly up-regulated the expression of transcripts and proteins involved in cell–cell adhesion (*Cldn5*, *Jam2*, and *Jcad*), in line with potential BBB tightening, while reducing the expression of *Cxcl12*, a chemokine critical for T cell entry to the CNS (22) (Fig. 3 *D* and *E*, and *SI Appendix*, Fig. S7). The gene expression changes in *Cldn5* (encodes claudin-5), *Jam2*, and *Cxcl12* and *Tjp1* (encodes ZO-1) were further confirmed by qPCR on corticosterone-treated primary mouse endothelial cells and bEnd.3 cells (Fig. 3*F* and *SI Appendix*, Fig. S8*A*).

Having established that the expression levels of BBB junctional molecules are increased by HSD and corticosterone, we investigated whether this results in altered permeability using in vitro and in vivo assays. Consistent with the increase of junctional molecules, treatment of primary mouse brain endothelial cell monolayers, or bEnd.3 cells with corticosterone decreased the permeability of FITC-dextran (Fig. 4*A* and *SI Appendix*, Fig. S8*B*). Most importantly, we also observed a reduced permeability of intravenously injected FITC-dextran into the brain of HSD-fed mice compared to C1000-fed mice (Fig. 4*B*). To establish the importance of tightened BBB on the EAE outcome, we injected HSD-fed OSE mice with pertussis toxin, a molecule known to open the BBB (23). The injection of pertussis toxin was sufficient to break the disease resistance in more than 80% of HSD-fed OSE mice with T cell infiltration into CNS driving demyelination, whereas none of the PBS-treated HSD-fed OSE mice developed EAE during the same period (Fig. 4 *C*–*E*).

In sum, our results show that dietary salt intake suppresses spontaneous EAE, a finding that starkly contrasts with previous studies that noted HSD-dependent exacerbation of disease in the actively induced EAE model (1–3). Unlike active EAE, where T cells are activated with antigen and BBB integrity is compromised by treatment with adjuvants and pertussis toxin, spontaneous EAE resembles human disease, MS, as it develops without exogenous manipulation. Like previous reports, we found that HSD-induced $T_H17$ cells are functionally capable in our model system. However, in the absence of BBB breakdown, they were unable to infiltrate the CNS to cause the disease. We found that elevated circulating corticosterone levels affected BBB permeability by promoting the expression of junctional and adhesion molecules thereby limiting the access of T cells to the CNS.

Does HSD affect human MS? While one study related sodium excretion with relapse rates in Argentinian MS patients (6), other evidence points to the opposite. Indeed, recent trials monitoring larger cohorts failed to note any aggravating effect of HSD intake in adult MS (7) and pediatric MS (24). It is tempting to invoke an epidemiological phenomenon in Japan, which relates to a drastic decrease of hypertension-related cardiovascular disease with a general reduction of dietary salt consumption (25). Importantly, in the same period, there was a robust increase of "Western-type" MS in Japan (26). While we are aware that this change may have numerous reasons, it is compatible with a protective, anti-autoimmune activity of moderately elevated salt uptake in humans. Our results also emphasize the multifaceted effects of HSD, and, in the case of clinically relevant issues, call for special care in selecting or combining representative experimental models for translation into clinical medicine.

## Materials and Methods

**Mice and Diet Regimen.** 2D2 × $IgH^{MOG}$ (OSE) (9) C57BL/6 mice, *Rag2*$^{-/-}$ C57BL/6, and wild-type C57BL/6 were bred at the animal facility of the Max Planck Institute of Biochemistry (Martinsried, Germany). Mice were fed either a chow diet, a control diet (C1000), or an HSD (C1036 supplemented with 4% NaCl) and were given autoclaved drinking water ad libitum. All diets used in the study were formulated by Altromin and γ-irradiated. Some experiments included 1% NaCl in drinking water. Unless otherwise specified, mice were raised on a regular rodent chow diet and switched to indicated diets after weaning. Mice were then fed with the indicated diets for 2 to 4 wk before the collection of organs, urine, caecal content, or blood. In some experiments, dietary treatment started from mating pairs, and mice were continued on the same diets after weaning. All animal procedures were in accordance with the guidelines of the Committee on Animals of the Max Planck Institute of Biochemistry and with approval from the Regierung von Oberbayern (Munich, Germany).

**EAE.** Spontaneous EAE was monitored in OSE mice up to 18 wk of age and the clinical disease was evaluated according to the standard scoring scheme (9). Active EAE was induced by injecting mice subcutaneously with 200 μL of emulsion containing 100 μg $MOG_{35–55}$ peptide (MEVGWYRSPFSRVVHLYRNGK) and 500 μg *Mycobacterium tuberculosis* strain H37 Ra (Difco) in incomplete Freund's adjuvant (Difco). Mice additionally received 400 ng pertussis toxin (Sigma-Aldrich) intraperitoneally (i.p.) on days 0 and 2 after immunization. For adoptive cell transfer EAE experiments, $5 \times 10^7$ total splenocytes from C1000- or HSD-fed OSE mice were isolated and injected intravenously (i.v.) into *Rag2*$^{-/-}$ mice. Clinical signs of EAE were assessed according to the standard scoring scheme (9).

**In Vivo Pertussis Toxin or Antibody Treatment.** OSE mice were weaned onto HSD and treatments were started 5 to 7 d after the diet switch. For the pertussis toxin treatment experiment, 400 ng pertussis toxin (Sigma-Aldrich) or phosphate-buffered saline (PBS) was administered i.p. once every week, for 4 wk. For the $T_{reg}$ cell depletion experiment, mice were injected i.p. with 250 μg anti-CD25 antibody (PC61) or rat IgG1 isotype control antibodies (GL113) once a week for 4 wk. Antibodies were purified from the hybridoma culture supernatants. Mice were monitored for clinical signs of EAE and scored according to the standard scoring scheme (9).

**Cell Isolation and Flow Cytometry.** Single-cell suspensions of splenocytes were prepared by mechanical disruption through 40-μm cell strainers (Corning). For the isolation of lamina propria lymphocytes, the small intestine and colon were collected in ice-cold Hanks' balanced salt solution (HBSS) buffered with 15 mM Hepes. After removal of Peyer's patches, fat tissue, and fecal content, the intestine was opened longitudinally and cut into small pieces. The intestinal fragments were washed three times for 15 min each by stirring in HBSS containing 5 mM ethylenediaminetetraacetic acid (EDTA),

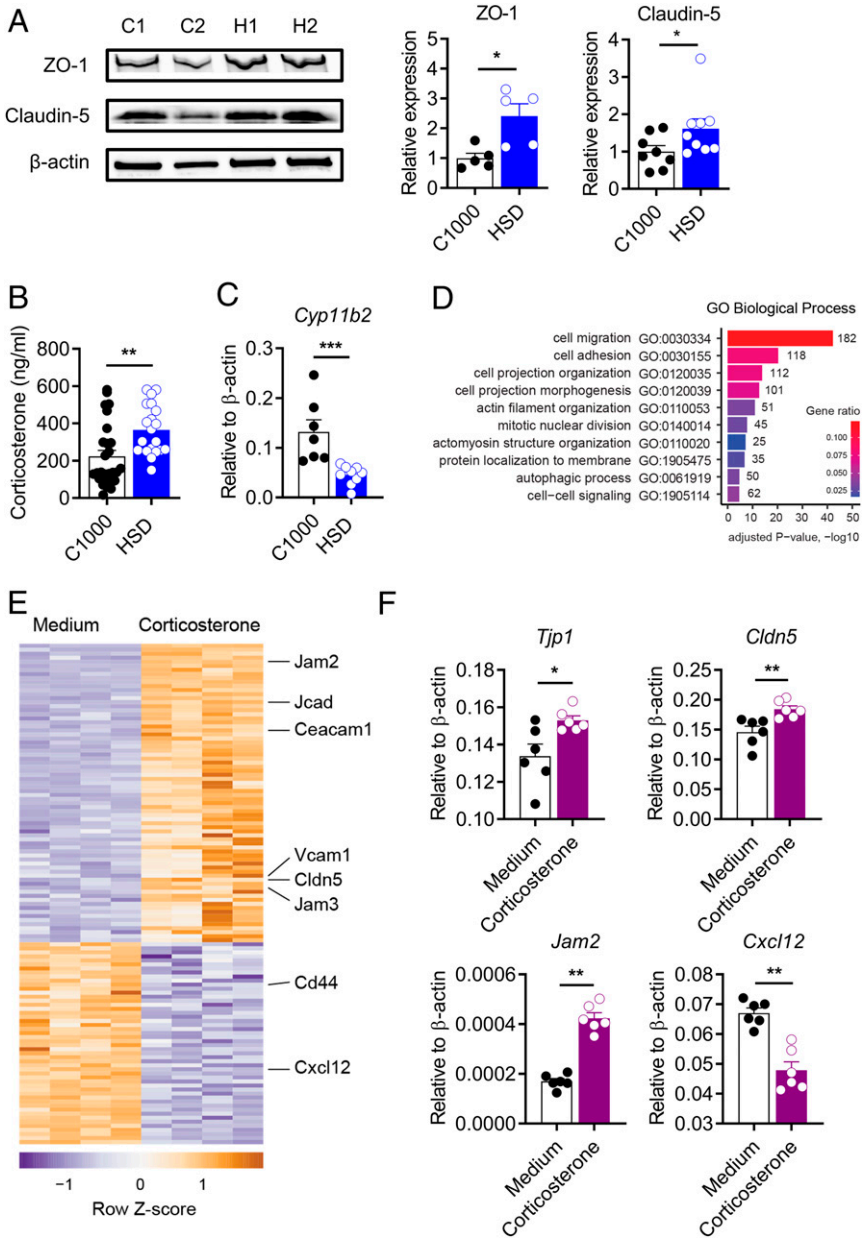


**Fig. 3.** HSD-induced corticosterone alters the expression of tight junction proteins in brain endothelial cells. (*A*) The expression levels of ZO-1 and claudin-5 proteins in sorted CD31$^+$ brain endothelial cells from OSE mice fed C1000 or HSD. Protein expression levels are normalized to β-actin. Representative blot images are shown on the *Left*. Each circle represents cells pooled from two mice. $n = 5$ to 9 per group. ZO-1 $^*P = 0.0317$, Claudin-5 $^*P = 0.0464$ (Mann–Whitney *U* test, two tailed). (*B*) Serum corticosterone concentrations in C1000 ($n = 27$)- or HSD ($n = 20$)-fed OSE mice quantified by ELISA. Data from sera collected across different litters are shown. Each circle represents an individual mouse. $^{**}P = 0.0011$ (Mann–Whitney *U* test, two tailed). (*C*) mRNA levels of *Cyp11b2* (aldosterone synthase) in the adrenal glands of OSE mice fed C1000 ($n = 7$) or HSD ($n = 9$). Each circle represents an individual mouse. The combined data from two independent experiments are shown. $^{***}P = 0.0002$ (Mann–Whitney *U* test, two tailed). (*D*) The effect of corticosterone treatment on the bEnd.3 brain endothelial cell transcriptome. Overrepresentation analysis (Gene Ontology [GO] gene sets, "Biological Process" category) of differentially expressed genes. The number of genes in each GO category is depicted next to the bars. (*E*) A heatmap of differentially expressed cell adhesion- and migration-related genes (ordered by log2 fold change). (*F*) mRNA levels of *Tjp1* (encodes ZO-1), *Cldn5* (encodes Claudin-5), *Jam2*, and *Cxcl12* in primary brain endothelial cells treated with corticosterone in vitro. Each circle represents an individual well. $n = 6$ per group. Representative data from two independent experiments are shown. Each circle represents an individual sample. $^*P = 0.0260$; $^{**}P = 0.0022$ (Mann–Whitney *U* test, two tailed).

15 mM Hepes and 5% fetal bovine serum (FBS). Next, intestinal pieces were washed once for 5 min by stirring in Roswell Park Memorial Institute (RPMI) medium (RPMI 1640; Sigma-Aldrich) containing 15 mM Hepes and 10% FBS, followed by enzymatic digestion with 100 U/mL collagenase VII (Sigma-Aldrich) in RPMI containing 15 mM Hepes and 5% FBS at 37 °C with stirring. The digested tissue was washed once in RPMI with 15 mM Hepes and 5% FBS. The pellet was resuspended in 5 mL of 40% Percoll (GE Healthcare Life Sciences), overlaid on 2.5 mL of 80% Percoll, and centrifuged at 2,000 × *g* for 20 min. Cells at the interface were collected and washed with RPMI containing 10% FBS.

For the isolation of lymphocytes from the brain and spinal cord, mice were perfused with PBS, and the brain and spinal cord were collected in RPMI containing 10% FBS. Tissue was forced through 100-μm cell strainers (Corning) and the homogenate was centrifuged at 300 × *g* for 10 min at 4 °C. The pellet was resuspended in 5 mL RPMI containing 10% FBS, mixed with 2.16 mL Percoll (density 1.123 g/mL), overlaid onto 5 mL Percoll (density 1.08 g/mL),

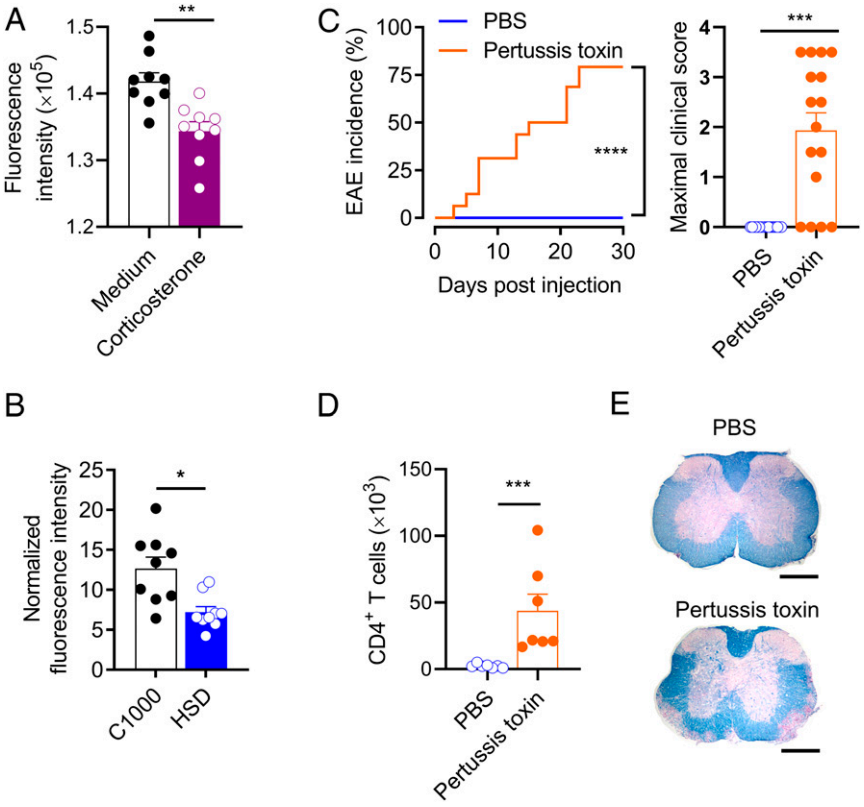


**Fig. 4.** Corticosterone treatment reduces BBB permeability. (*A*) Permeability to FITC-dextran in vitro in primary brain endothelial cells treated with corticosterone. The combined data from two independent experiments are shown. Each circle represents an individual sample. $n = 9$ per group. $^{**}P = 0.0012$ (Mann–Whitney *U* test, two tailed). (*B*) BBB permeability to FITC-dextran in vivo in C57BL/6 mice fed C1000 ($n = 9$) or HSD ($n = 9$). The fluorescence values normalized to the tissue weight and serum FITC-dextran levels (ng per mg brain tissue/μg per μL serum) are shown. The combined data from two independent experiments are shown. Each circle represents an individual mouse. $^{*}P = 0.0106$ (Mann–Whitney *U* test, two tailed). (*C*) Incidence of EAE in HSD-fed OSE mice treated with pertussis toxin ($n = 16$) or PBS ($n = 18$) (*Left*) and maximal clinical score attained by mice that developed EAE (*Right*). The combined data from three independent experiments are shown. Each circle represents an individual mouse. $^{****}P = 0.0001$ (Gehan–Breslow–Wilcoxon test). $^{***}P = 0.0005$ (Wilcoxon signed-rank test). (*D*) Flow cytometry analysis of spinal cord-infiltrating T cells from HSD-fed OSE mice that received PBS or pertussis toxin. The total number of $CD4^+$ T cells in the spinal cord is shown. The combined data from two independent experiments are shown. Each circle represents an individual mouse. $n = 7$ per group. $^{***}P = 0.0006$ (Mann–Whitney *U* test, two tailed). (*E*) Representative images of spinal cord sections stained with luxol fast blue from PBS ($n = 2$) and pertussis-treated ($n = 2$) groups. (Scale bar, 500 μm.)

and centrifuged at 1,200 × *g* for 30 min. The cells at the interface were collected and washed with RPMI containing 10% FBS.

For the detection of cell surface markers, cells were stained in a flow cytometry buffer (PBS supplemented with 1% bovine serum albumin (BSA; Carl-Roth) and 0.1% $NaN_3$) with Fixable Viability Dye-eFluor 780 (Thermo Fisher Scientific) and the following antibodies: anti-CD4-PerCP-Cy5.5 or Brilliant Violet 711 (RM4-5), anti-CD45-eFluor 450 or Brilliant Violet 785 (30-F11), anti-CD19-FITC or PE (1D3), anti-CD11b-PE-Cy7 or PE (M1/70), anti-Ly6G-APC (1A8), and anti-Ly6C-FITC (AL-21). For intracellular cytokine staining, cells were activated with 50 ng/mL phorbol 12-myristate 13-acetate (PMA) (Sigma-Aldrich) and 500 ng/mL ionomycin (Sigma-Aldrich) in the presence of 5 μg/mL brefeldin A (Sigma-Aldrich) for 4 h at 37 °C. After surface staining, cells were fixed and permeabilized using the Transcription Factor Staining Buffer Set (Thermo Fisher Scientific) and stained intracellularly using the following antibodies: anti-IL-17-APC (TC11-18H10) and anti-IFNγ-FITC, PE-Cy7 or Brilliant Violet 421 (XMG1.2), or anti-Foxp3-APC (FJK-16s). Antibodies were purchased from BD Biosciences, Biolegend, or Thermo Fisher Scientific. Cells were acquired on a FACS Canto (BD Biosciences) or FACS Fortessa (BD Biosciences) and analyzed using FlowJo software (TreeStar).

**Proliferation Assay.** Spleen cells were briefly incubated with 0.83% $NH_4Cl$ to remove red blood cells and washed once in RPMI and once in PBS. Cells were labeled with 10 μM Cell Proliferation Dye eFluor 450 (Thermo Fisher Scientific) for 10 min at room temperature, washed in PBS, resuspended in RPMI containing 10% FBS, and stimulated with recombinant MOG protein (rMOG) at the indicated concentrations in a 96-well plate ($2 \times 10^5$ cells per well) for 60 h. Cells were stained with anti-CD4-PerCP-Cy5.5, anti-B220-APC, and acquired on a FACS Canto (BD Biosciences). The proliferation was defined based on the reduced eFluor 450 fluorescence relative to nonstimulated control cells.

**In Vitro Suppression Assay.** $CD4^+$ T cells from lymph nodes and spleen were isolated using MojoSort mouse $CD4^+$ T cell isolation kit (Biolegend), stained with anti-CD4-PerCP-Cy5.5 (RM4-5) and anti-CD25 PE (PC61) antibodies and $CD4^+CD25^-$ effector T cells ($T_{eff}$) or $CD4^+CD25^+$ regulatory T cells ($T_{reg}$) were sorted using FACS Aria III (BD Biosciences). For the suppression assay, $T_{eff}$ cells were labeled with Cell Proliferation Dye eFluor 450 (Thermo Fisher Scientific) and $10^5$ labeled cells were cocultured with $5 \times 10^4$ bone marrow-derived dendritic cells, 1 μg/mL InVivoMAb anti-CD3 (145-2C11, BioXCell) at varying $T_{reg}$:$T_{eff}$ ratios. Proliferation was analyzed by flow cytometry after 4 d.

**Isolation of Brain Endothelial Cells.** Brain endothelial cells were isolated as previously described (27). In brief, brain tissue was minced mechanically and digested with collagenase II (Sigma-Aldrich) for 50 min at 37 °C and pellets were resuspended with 25% BSA followed by centrifugation for 30 min at 1,000 × *g* to remove myelin. To prepare single-cell suspensions, pellets were digested with 1 mg/mL collagenase/dispase (Sigma-Aldrich) solution, stained with Fixable Viability Dye-eFluor 780, anti-CD31-PE (MEC13.3), and anti-CD45- Brilliant Violet 421 (30-F11) antibodies, and sorted using FACS Aria III. For endothelial cell cultivation, enzyme-digested cells were resuspended in a Dulbecco's modified Eagle medium (DMEM)-F12 medium containing 10% FBS, penicillin/streptomycin, L-glutamine, and endothelial-cell growth supplement (Thermo Fisher Scientific) and cultured in a 0.02% collagen-coated (Sigma-Aldrich) plate. The next day the plate was washed eight times with DMEM-F12 and cells were cultured with 4 μg/mL puromycin (InvivoGen) in

DMEM-F12 medium containing 10% FBS, penicillin/streptomycin, L-glutamine, and endothelial-cell growth supplement (Thermo Fisher Scientific) for 2 d and cultured without puromycin for 3 more days.

**In Vitro FITC-Dextran Permeability Assay.** Brain endothelioma bEnd.3 cells were cultured in DMEM, supplemented with 10% FBS, and harvested by detachment with TrypLE (Thermo Fisher Scientific). For in vitro permeability assay, bEnd.3 cells or isolated primary endothelial cells were seeded on fibronectin-coated (7 μg/mL, Sigma-Aldrich) or collagen-precoated Transwell plates (0.4 μm pore size; Thermo Fisher Scientific) and cultured for 3 d. Cells were then incubated with 5 μM corticosterone (Sigma-Aldrich) and 1 mg/mL 40-kDa FITC-dextran (Sigma-Aldrich) for 20 h. Medium from the receiver tray was collected, diluted to 1:20 in PBS, and fluorescence was measured with a spectrophotometer (Perkin-Elmer) at an excitation wavelength of 490 nm and emission of 529 nm.

**Western Blot.** Sorted brain $CD31^+$ endothelial cells were washed with PBS and cell pellets were lysed with Radioimmunoprecipitation assay (RIPA) buffer (Serva) with protease and phosphatase inhibitor cocktail (Thermo Fisher Scientific) and an equal volume of SDS-containing sample buffer (Sigma-Aldrich) was added and boiled. Total proteins were separated on a 4 to 15% SDS-polyacrylamide gel and transferred onto a nitrocellulose membrane (Bio-Rad). After blocking with 5% nonfat dry milk in TBS-T (Tris-buffered saline with 0.1% Tween 20), immunoblots were incubated with primary antibodies overnight, washed in TBS-T, further incubated with horseradish peroxidase (HRP)-conjugated anti-rabbit IgG antibody (Advansta) for 1 h, and visualized with chemiluminescence (Clarity Western ECL substrate, Bio-Rad) on a Chemidoc MP imaging system (Bio-Rad). The antibodies used for immunoblot analysis were against ZO-1 (Thermo Fisher Scientific), Claudin-5 (Sigma-Aldrich), and β-actin-HRP (Biolegend). The densitometric analysis of each protein signal was obtained using the Molecular Imager Chemidoc (Bio-Rad) and normalized against β-actin expression.

**Real-Time PCR.** Total RNA was isolated from sorted brain $CD31^+$ endothelial cells using the Nucleospin RNA mini kit (Macherey Nagel) followed by conversion into cDNA using Maxima H– cDNA synthesis kit (Thermo Fisher Scientific) according to the manufacturer's instructions. mRNA levels were measured using predesigned qPCR assays with FAM-labeled gene-specific probes together with HEX-labeled β-actin or JOE-labeled GAPDH probes. Except for GAPDH, all other primers/probes were obtained from IDT as predesigned assays. *Cldn5* – Mm.PT.58.33394738; *Tjp1* (ZO-1) – Mm.PT.58.12952721; *Actb* (β-actin) – Mm.PT.39a.22214843.g; *Jam2* – Mm.PT.58.5384170; *Cxcl12* – Mm.PT.58.32677664; *Hsd3b1* – Mm.PT.58.43898780; *Hsd11b1* – Mm.PT.58.32968808; *Cyp21a1* – Mm.PT.58.42183110; *Cyp11a1* – Mm.PT.58.14210705; *Cyp11b1* – Mm.PT.58.41798181; and *Cyp11b2* – Mm.PT.58.10194955. GAPDH primer sequences: mGAPDH-forward, TCACCACCATGGAGAAGGC; mGAPDH-reverse, GCTAAGCAGTTGGTGGTGCA; mGAPDH-probe, JOE-ATGCCCCCATGTTTGTGATGG GTG T-BHQ.

**Enzyme-Linked Immunosorbent Assay.** Blood was collected by retro-orbital bleeding into serum gel tubes (Sarstedt) and centrifuged at 8,000 × *g* for 5 min to separate serum. Serum samples were frozen at −20 °C until further use. Colon explants (1 cm long) were collected in ice-cold HBSS buffered with 15 mM Hepes. After removal of fat tissue and fecal content, the explants were washed for 15 min three times by stirring in HBSS containing 5 mM EDTA, 15 mM Hepes, and 5% FBS. The explants were then cultured in RPMI containing 5% FBS overnight and the supernatants were collected and frozen at −20 °C until further use. Caecal content was collected and weighed, and 1 mL methanol was added per 500 mg caecal content. Samples were then vigorously vortexed for 1 min and centrifuged at 10,000 × *g* for 10 min. The supernatants were collected and stored at −20 °C until further use.

IgE levels were measured using a mouse serum IgE enzyme-linked immunosorbent assay (ELISA) kit (Biolegend). Total IgG was measured using a mouse serum IgG ELISA kit (Thermo Fisher Scientific). Corticosterone was measured with the parameter Corticosterone assay kit (R&D Biosystems). To detect MOG-reactive antibodies, 96-well plates were coated with 20 μg/mL recombinant MOG protein overnight at 4 °C. After washing with PBS-T (0.1% Tween 20 in PBS) and blocking with 10% FBS in PBS for 2 h, serum was added at different dilutions (diluted $10^4$ and $10^5$ fold in 10% FBS in PBS) to a final volume of 100 μL and incubated for 2 h. After washing, biotin-labeled antibodies against $IgG1^a$ (10.9), $IgG2a^a$ (8.3), or $IgM^a$ (DS-1), all from BD Pharmingen, were added (1 μg/mL) for 1 h, then washed and incubated with HRP-labeled streptavidin (Biolegend) for another hour. Finally, 3,3′,5,5′-tetramethylbenzidine (TMB) substrate solution (Biolegend) was added and the reaction was stopped with 1N $H_2SO_4$. Plates were measured in a spectrophotometer (Perkin-Elmer) at 450 nm.

**Urinary Sodium Measurement.** Sodium concentration in urine was measured using a sodium enzymatic assay (Diazyme) according to the manufacturer's instructions.

**In Vivo Permeability Assay.** C1000- or HSD-fed mice were injected with 2 mg 4-kDa FITC-dextran (Sigma-Aldrich) i.v. in 200 μL PBS. After 20 min, blood was collected by retro-orbital bleeding, mice were perfused with PBS, and the brain was collected. The tissues were weighed and homogenized in 1.5 mL PBS. The homogenates were centrifuged at 10,000 × *g* at 4 °C for 10 min, the supernatant was collected, and the centrifugation was repeated to ensure complete removal of tissue and myelin debris. FITC-dextran fluorescence was measured in the supernatants with a spectrophotometer (Perkin-Elmer) at excitation of 485 nm and an emission of 530 nm. A total of 4 kDa FITC-dextran in PBS (2.5 μg/mL, twofold dilution series) was used as a standard for concentration calculations. The values were normalized to tissue weight and FITC-dextran levels in the serum.

**Proteomics.** bEnd.3 cells were cultured overnight in a six-well plate, then treated with 5 μM corticosterone for 24 h, collected, washed with PBS, and the cell pellets ($10^6$ cells) were snap-frozen and stored at −80 °C. Cell pellets were lysed in 400 μL of lysis buffer containing 1% sodium deoxycholate, 40 mM 2-chloroacetamide (Sigma-Aldrich), 10 mM Tris(2-carboxyethyl) phosphine (TCEP; Thermo Fisher Scientific) in 100 mM Tris, pH 8.0, at 95 °C for 2 min and then sonicated 10 times for 30 s at high intensity using a Bioruptor Plus sonication system (Diogenode). The lysis and sonication steps were performed twice. Samples were diluted 1:4 in mass spectrometry (MS) grade water (VWR International) and digested for 4 h at 37 °C with 1 μg of LysC and overnight at 37 °C with 3 μg trypsin (Promega). The solution of peptides was acidified with trifluoroacetic acid (TFA; Merck) to a final concentration of 1%, followed by purification via SCX StageTips (28) (Thermo Fisher Scientific), washed with 1% TFA in isopropanol, followed by a second wash with 0.2% TFA, eluted as one fraction with 80% acetonitrile and 5% ammonia (Merck). Samples were vacuum-dried and resuspended in 6 μL of buffer A (0.1% formic acid [Carl-Roth] in MS grade water) before loading.

Peptides were loaded onto a column (30 cm, inner diameter of 75 μm) packed in-house with ReproSil-Pur C18-AQ 1.9-μm beads (Dr. Maisch) via the autosampler of the Thermo Easy-nLC 1000 (Thermo Fisher Scientific) at 60 °C. Using the nanoelectrospray interface, eluting peptides were directly sprayed onto the benchtop Orbitrap mass spectrometer Q Exactive HF (Thermo Fisher Scientific). Peptides were loaded in buffer A (0.1% (vol/vol) formic acid) at 250 nL/min and the percentage of buffer B (80% acetonitrile, 0.1% formic acid) was ramped to 30% over 120 min, followed by a ramp to 60% over 10 min, then to 95% over the next 5 min and percentage of buffer B was maintained at 95% for another 5 min. The mass spectrometer was operated in a data-dependent mode with survey scans from 300 to 1,750 *m/z* (resolution of 60,000 at $m/z = 200$), and up to 15 of the top precursors were selected and fragmented using higher-energy collisional dissociation (with normalized collision energy equal to 28). The $MS^2$ spectra were recorded at a resolution of 15,000 (at $m/z = 200$). Automatic gain control (AGC) target for $MS^1$ and $MS^2$ scans were set to $3e^6$ and $1e^5$, respectively, within a maximum injection time of 100 ms for $MS^1$ and 25 ms for $MS^2$ scans. Dynamic exclusion was set to 30 ms.

Raw data were processed using the MaxQuant computational platform (29) with standard settings. The peak list was searched against the reviewed UniProt mouse proteome database (downloaded March 7, 2019) with an allowed precursor mass deviation of 4.5 ppm and an allowed fragment mass deviation of 20 ppm. MaxQuant by default enables individual peptide mass tolerances, which was used in the search. Cysteine carbamidomethylation was set as static modification, and methionine oxidation and N-terminal acetylation as variable modifications.

Downstream proteomics analyses and visualizations were performed in the R environment (version 3.6.1) running under Windows 10 x64. Data filtering, normalization, and differential expression were performed using the DEP package (version 1.8.0) (30), in which label-free quantification (LFQ) intensities from the "proteinGroups" file were used as input. The data were filtered to remove reverses, potential contaminants, and missing values (only the proteins that are identified in four out of five replicates of at least one condition were kept for further analyses). The LFQ intensities were normalized by applying the variance stabilizing transformation (31). The missing values were imputed using random draws from a Gaussian distribution centered around a minimal value (the missing not at random [MNAR] type of imputation methods, the "MinProb" function with $q = 0.01$). For differential expression analysis, the groups of interest were contrasted using a differential enrichment test based on protein-wise linear models and empirical Bayes statistics originally implemented in the limma package (32). Proteins

with adjusted *P* values below 0.01 and a fold change of at least 20% were considered as differentially expressed.

**mRNA-Seq.** mRNA sequencing libraries were prepared from 1 μg of total RNA of each sample using the NEBNext Ultra II Directional RNA Library Prep Kit for Illumina (New England Biolabs) with NEBNext Poly(A) mRNA Magnetic Isolation Module (New England Biolabs). Total RNA and the final library quality controls were performed using Qubit Flex Fluorometer (Thermo Fisher Scientific) and a 2100 Bioanalyzer Instrument (Agilent) before and after library preparation. Paired-end sequencing was performed on Illumina NextSEq. 500 (2x 43 base pair reads). Samples were multiplexed and sequenced on one High Output Kit v2.5 to reduce a batch effect. Binary base call (BCL) raw data were converted to FASTQ data and demultiplexed by bcl2fastq Conversion Software, which generated 20 to 40 million reads per sample.

Pseudoalignment and gene-level quantification were performed with Kallisto (version 0.46.1) (33); *Mus musculus* genome assembly version mm10/GRCm38 was used for indexing with 100 bootstraps. Gene-level abundance estimates were imported to DESeq2 (version 1.26.1) (34) with tximport (version 1.14.2) (35) for differential expression analysis. Genes with at least a 20% change in expression, adjusted *P* value below 0.01, and average expression above 100 abundance estimates were considered as differentially expressed. The transcripts-to-genes map was generated for the Ensembl v96 *M. musculus* transcriptome (released in 2019; https://github.com/pachterlab/kallisto-transcriptome-indices/releases). Variance stabilizing transformation was applied to normalize pseudocounts for downstream visualizations.

For both mRNA-seq and proteomics data, overrepresented gene ontology (GO) gene sets (the "Biological Process" category) among differentially expressed genes or proteins were detected using clusterProfiler (version 3.14.3) (36) and filtered by semantic similarity (using an information content-based method by Schlicker et al. (37) with a cutoff of 0.5 (GOSemSim, version 2.12.1) (38) to simplify the GO term redundancy. Subsequent data filtering and visualizations were performed in the R environment using the tidyverse packages and pheatmap.

**Histopathology.** Spinal cord samples were fixed with 4% paraformaldehyde in PBS, embedded in paraffin, and 5-μm-thick sections were prepared using a microtome. Slides were stained with Luxol Fast Blue (Sigma-Aldrich) overnight at 56 °C, differentiated with 0.1% $Li_2CO_3$, and counterstained with Periodic Acid-Schiff (Carl-Roth).

**Statistical Analysis.** GraphPad Prism 8 or 9 (GraphPad Software, Inc.) was used for all statistical analyses. Information on statistical tests used for analysis is mentioned in figure legends. *P* values below 0.05 were considered significant. Bars depict mean ± SE of mean.

**Data Availability.** The shotgun mass spectrometry data have been deposited in the ProteomeXchange Consortium (proteomecentral.proteomexchange.org) via the Proteomics Identification Database (PRIDE) partner repository (39) with the dataset identifier PXD022166. Raw mRNA-seq data and estimated counts are available at the SRA (BioProject PRJNA670426, Sequence Read Archive (SRA) accession number SRP287985) and Gene Expression Omnibus (GEO) (GSE159756) repositories, respectively. Code for downstream analyses, nonadjusted figures, and supplemental data (differential expression results, overrepresentation analysis results) are available at GitHub, github.com/krishnamoorthy-lab/salt.

**ACKNOWLEDGMENTS.** We thank Hartmut Wekerle and Kerstin Berer for the pilot experiments and discussions. We thank Birgit Kunkel and Jeeva Varadarajulu for their technical assistance. We thank the Mass Spectrometry and NGS Core Facilities at the Max Planck Institute of Biochemistry for performing sample analysis for proteomics and mRNA-seq experiments. This work was funded by European Research Council Starting Grant (GAMES; 635617), German Research Foundation (DFG) Grant SFB TR-128 (Project A1), and by the Max Planck Society.

1. M. Kleinewietfeld *et al*., Sodium chloride drives autoimmune disease by the induction of pathogenic TH17 cells. *Nature* **496**, 518–522 (2013).
2. C. Wu *et al*., Induction of pathogenic TH17 cells by inducible salt-sensing kinase SGK1. *Nature* **496**, 513–517 (2013).
3. N. Wilck *et al*., Salt-responsive gut commensal modulates $T_H17$ axis and disease. *Nature* **551**, 585–589 (2017).
4. World Health Organization, Guideline: Sodium intake for adults and children (2012). https://www.who.int/publications/i/item/9789241504836. Accessed 5 March 2021.
5. F. H. Messerli, L. Hofstetter, S. Bangalore, Salt and heart disease: A second round of "bad science"? *Lancet* **392**, 456–458 (2018).
6. M. F. Farez, M. P. Fiol, M. I. Gaitán, F. J. Quintana, J. Correale, Sodium intake is associated with increased disease activity in multiple sclerosis. *J. Neurol. Neurosurg. Psychiatry* **86**, 26–31 (2015).
7. A. Ascherio, K. L. Munger, People with MS should consume a low-salt diet - NO. *Mult. Scler.* **22**, 1779–1781 (2016).
8. C. Confavreux, S. Suissa, P. Saddier, V. Bourdès, S. Vukusic; Vaccines in Multiple Sclerosis Study Group, Vaccinations and the risk of relapse in multiple sclerosis. *N. Engl. J. Med.* **344**, 319–326 (2001).
9. G. Krishnamoorthy, H. Lassmann, H. Wekerle, A. Holz, Spontaneous opticospinal encephalomyelitis in a double-transgenic mouse model of autoimmune T cell/B cell cooperation. *J. Clin. Invest.* **116**, 2385–2392 (2006).
10. T. Korn, M. Oukka, V. Kuchroo, E. Bettelli, Th17 cells: Effector T cells with inflammatory properties. *Semin. Immunol.* **19**, 362–371 (2007).
11. R. Jain *et al*., Interleukin-23-induced transcription factor Blimp-1 promotes pathogenicity of T helper 17 cells. *Immunity* **44**, 131–142 (2016).
12. S. Huber, N. Gagliani, R. A. Flavell, Life, death, and miracles: Th17 cells in the intestine. *Eur. J. Immunol.* **42**, 2238–2245 (2012).
13. E. Esplugues *et al*., Control of $T_H17$ cells occurs in the small intestine. *Nature* **475**, 514–518 (2011).
14. J. Matthias *et al*., Salt generates antiinflammatory Th17 cells but amplifies pathogenicity in proinflammatory cytokine microenvironments. *J. Clin. Invest.* **130**, 4587–4600 (2020).
15. K. Kitada *et al*., High salt intake reprioritizes osmolyte and energy metabolism for body fluid conservation. *J. Clin. Invest.* **127**, 1944–1959 (2017).
16. N. Rakova *et al*., Increased salt consumption induces body water conservation and decreases fluid intake. *J. Clin. Invest.* **127**, 1932–1943 (2017).
17. M. H. Alderman *et al*., Association of the renin-sodium profile with the risk of myocardial infarction in patients with hypertension. *N. Engl. J. Med.* **324**, 1098–1104 (1991).
18. K. Jobin *et al*., A high-salt diet compromises antibacterial neutrophil responses through hormonal perturbation. *Sci. Transl. Med.* **12**, eaay3850 (2020).
19. I. Cima *et al*., Intestinal epithelial cells synthesize glucocorticoids and regulate T cell activation. *J. Exp. Med.* **200**, 1635–1646 (2004).
20. X. Yan *et al*., Intestinal flora modulates blood pressure by regulating the synthesis of intestinal-derived corticosterone in high salt-induced hypertension. *Circ. Res.* **126**, 839–853 (2020).
21. A. Mukherji, A. Kobiita, T. Ye, P. Chambon, Homeostasis in intestinal epithelium is orchestrated by the circadian clock and microbiota cues transduced by TLRs. *Cell* **153**, 812–827 (2013).
22. E. E. McCandless, R. S. Klein, Molecular targets for disrupting leukocyte trafficking during multiple sclerosis. *Expert Rev. Mol. Med.* **9**, 1–19 (2007).
23. M. K. Racke, W. Hu, A. E. Lovett-Racke, PTX cruiser: Driving autoimmunity via TLR4. *Trends Immunol.* **26**, 289–291 (2005).
24. B. Nourbakhsh *et al*.; Network of Pediatric Multiple Sclerosis Centers, Dietary salt intake and time to relapse in paediatric multiple sclerosis. *J. Neurol. Neurosurg. Psychiatry* **87**, 1350–1353 (2016).
25. K. Miura *et al*.; NIPPON DATA80/90 Research Group, Dietary salt intake and blood pressure in a representative Japanese population: Baseline analyses of NIPPON DATA80. *J. Epidemiol.* **20** (suppl. 3), S524–S530 (2010).
26. T. Yamamura, S. Miyake, "Diet, gut flora, and multiple sclerosis: Current research and future perspectives" in *Multiple Sclerosis Immunology: A Foundation for Current and Future Treatments*, T. Yamamura, B. Gran, Eds. (Springer, New York, NY, 2013), pp. 115–126.
27. C. J. Czupalla, H. Yousef, T. Wyss-Coray, E. C. Butcher, Collagenase-based single cell isolation of primary murine brain endothelial cells using flow cytometry. *Bio Protoc.* **8**, e3092 (2018).
28. J. Rappsilber, M. Mann, Y. Ishihama, Protocol for micro-purification, enrichment, pre-fractionation and storage of peptides for proteomics using StageTips. *Nat. Protoc.* **2**, 1896–1906 (2007).
29. J. Cox, M. Mann, MaxQuant enables high peptide identification rates, individualized p.p.b.-range mass accuracies and proteome-wide protein quantification. *Nat. Biotechnol.* **26**, 1367–1372 (2008).
30. X. Zhang *et al*., Proteome-wide identification of ubiquitin interactions using UbIA-MS. *Nat. Protoc.* **13**, 530–550 (2018).
31. W. Huber, A. von Heydebreck, H. Sültmann, A. Poustka, M. Vingron, Variance stabilization applied to microarray data calibration and to the quantification of differential expression. *Bioinformatics* **18** (suppl. 1), S96–S104 (2002).
32. M. E. Ritchie *et al*., Limma powers differential expression analyses for RNA-sequencing and microarray studies. *Nucleic Acids Res.* **43**, e47 (2015).
33. N. L. Bray, H. Pimentel, P. Melsted, L. Pachter, Near-optimal probabilistic RNA-seq quantification. *Nat. Biotechnol.* **34**, 525–527 (2016).
34. M. I. Love, W. Huber, S. Anders, Moderated estimation of fold change and dispersion for RNA-seq data with DESeq2. *Genome Biol.* **15**, 550 (2014).
35. C. Soneson, M. I. Love, M. D. Robinson, Differential analyses for RNA-seq: Transcript-level estimates improve gene-level inferences. *F1000 Res.* **4**, 1521 (2015).
36. G. Yu, L. G. Wang, Y. Han, Q. Y. He, clusterProfiler: An R package for comparing biological themes among gene clusters. *OMICS* **16**, 284–287 (2012).
37. A. Schlicker, F. S. Domingues, J. Rahnenführer, T. Lengauer, A new measure for functional similarity of gene products based on Gene Ontology. *BMC Bioinformatics* **7**, 302 (2006).
38. G. Yu *et al*., GOSemSim: An R package for measuring semantic similarity among GO terms and gene products. *Bioinformatics* **26**, 976–978 (2010).
39. Y. Perez-Riverol *et al*., The PRIDE database and related tools and resources in 2019: Improving support for quantification data. *Nucleic Acids Res.* **47**, D442–D450 (2019).